ACS APPLIED ENGINEERING MATERIALS

pubs.acs.org/acsaenm Article

Scaling-Up Seeded Hydrothermal Nanowire Synthesis on Non-planar Surfaces Using a Flow Reactor

Alondra M. Ortiz-Ortiz, Andrew J. Gayle, Jing Wang, Hannah R. Faustyn, Daniel Penley, Caleb Sherwood, Anish Tuteja, and Neil P. Dasgupta*

Cite This: *ACS Appl. Eng. Mater.* 2023, 1, 1583−1592 Read Online

ACCESS | Metrics & More | Article Recommendations | Supporting Information

ABSTRACT: While many nanomaterial synthesis processes have been demonstrated at the laboratory scale, grand challenges remain at the nanomanufacturing frontier, where it is necessary to maintain tunable material structure and properties at large length scales using high-throughput, low-cost, and sustainable processes. Seeded hydrothermal synthesis is widely used to generate tunable nanostructures with controlled geometric parameters. In this study, we used atomic layer deposition to deposit precise and conformal seed layers which were subsequently processed using a customized hydrothermal flow reactor. The reactor design allows for control of the solution temperature profile in space and time, as well as the solution flow profile. Recirculation of the hydrothermal growth solution enables reduction of the chemical waste by 77−92% compared to a single pass flow reactor. This "surface-directed assembly" process allows for the growth of vertically aligned zinc oxide (ZnO) nanowires (NWs) directly onto macroscopic (cm-scale) non-planar surfaces. We quantify the uniformity of the NW morphology using scanning electron microscopy and UV absorption measurements. The NWs were further functionalized to form superhydrophobic and optically transparent surface coatings along a curved glass dome substrate. The surface coatings were shown to significantly reduce the rate of biofouling from marine algae by ∼75%. This demonstrates a pathway for the scale-up of hydrothermal synthesis processes with a variety of applications in the biological and environmental fields, including medical devices and optical and oceanographic sensors.

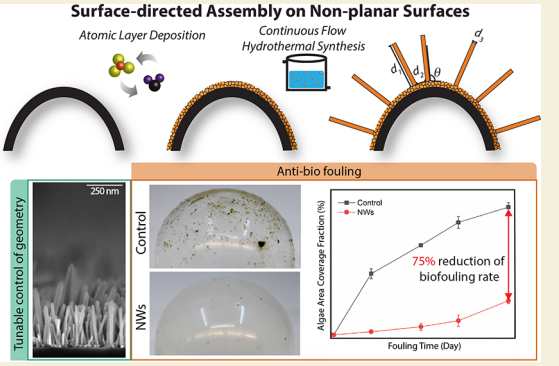

KEYWORDS: *nanomanufacturing, nanowires, atomic layer deposition, hydrothermal synthesis, superhydrophobic, anti-fouling*

1. INTRODUCTION

In recent years, there has been significant development of new processes for the design and manufacturing of complex nanostructured materials for use in the biological, environmental, and energy fields.[1−6] To this end, a variety of bottom-up and top-down methods have been developed for the fabrication of nanomaterials.[7−12] However, many grand challenges remain at the nanomanufacturing frontier, where it is challenging to simultaneously maintain the tunability, reproducibility, and scalability of rationally designed nanomaterials using high-throughput, low-cost, and sustainable processes.[13−18]

A facile technique for scalable synthesis of nanomaterials is atmospheric-pressure hydrothermal synthesis of ZnO nanowires (NWs), which occurs under mild reaction conditions. ZnO is a non-toxic functional material with useful electronic, piezoelectric, and optical properties, which enable its use in a range of applications including sensors and actuators, optoelectronic devices, and energy conversion and storage.[13,19−25] Additionally, ZnO nanostructures have demonstrated antimicrobial/antifouling properties attributed to the generation of Zn^{+2} ions and reactive oxygen species.[26] Through the incorporation of a "seed" layer on a substrate surface followed by hydrothermal synthesis, ZnO nanostructures can be grown into hierarchical assemblies, where the geometric properties of the resulting nanostructures are controlled by the crystallographic properties of the seed layer.[27]

We have previously demonstrated that by using atomic layer deposition (ALD) to deposit these seed layers with sub-monolayer precision, we can programmably tune the geometric parameters of the resulting ZnO nanostructures, which we refer to here as "surface-directed assembly" (Scheme 1).[5,28−30] ALD is a vapor-phase thin-film deposition technique based on the sequential and cyclic exposure of a substrate to precursor molecules that react in a self-limiting manner.[28,31] Owing to the layer-by-layer growth mode of ALD, the film thickness and composition can be controlled with sub-nanometer preci-

Received: March 21, 2023
Accepted: May 2, 2023
Published: May 18, 2023

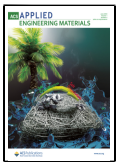

https://doi.org/10.1021/acsaenm.3c00129
ACS Appl. Eng. Mater. 2023, 1, 1583−1592

Scheme 1. Surface-Directed Assembly Process

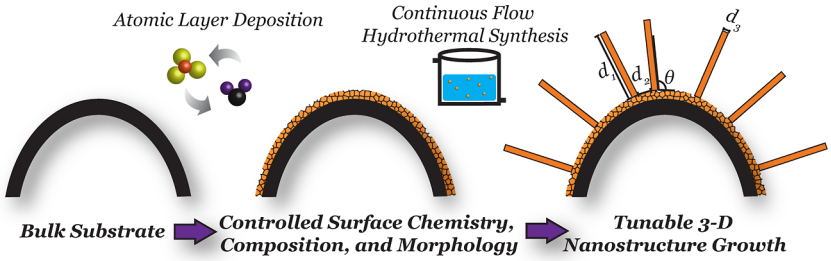

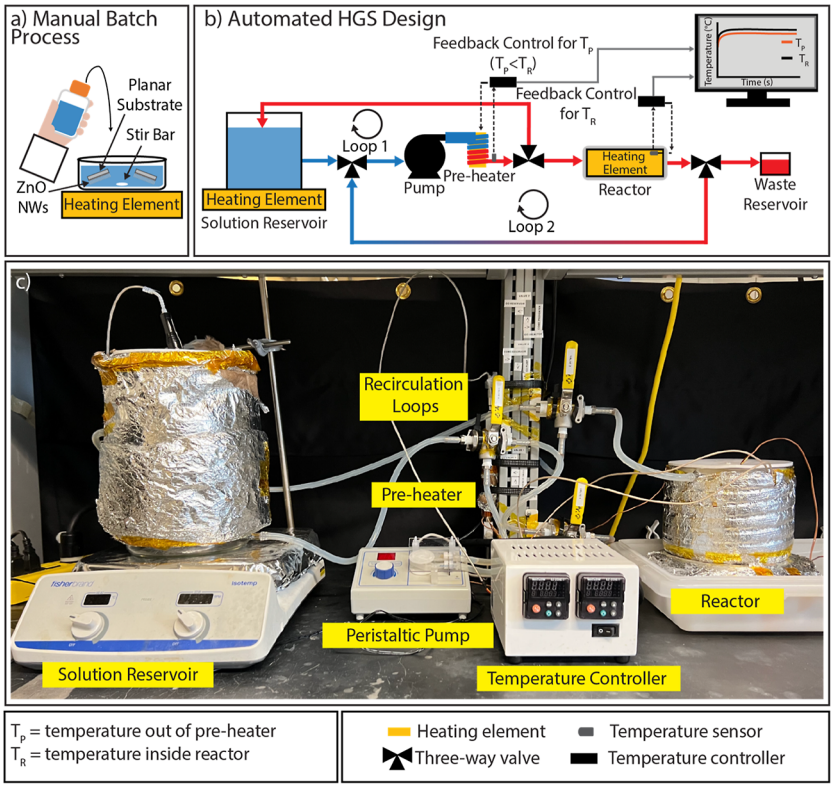

Figure 1. (a) Manual hydrothermal growth process in a batch reactor. (b) Design of the flow-based HGS used in this study. (c) Photograph of the HGS and its main components.

sion.[32,33] Furthermore, the uniformity and conformality of ALD films on high-aspect-ratio surfaces can be significantly higher than line-of-sight techniques such as physical and chemical vapor deposition, which has resulted in ALD being a key enabling technology in semiconductor manufacturing.[7,34,35] Additionally, the relatively low temperatures and roughing vacuum pressures used in ALD enable seeded hydrothermal synthesis to be performed on a variety of substrates, including flexible polymers, porous templates, and even biological materials.[28]

We have previously reported that the geometric properties (orientation, diameter, and spacing) of ZnO NWs can be rationally controlled by the crystallographic properties and microstructure of the ZnO seed layer, which can be directly tuned by varying the number of ALD cycles.[28] Additionally, the spacing between the NWs can be further tuned by depositing a sub-monolayer overcoat of titanium dioxide (TiO_2) over the ZnO seed layer, which can be used to tune the nucleation density by blocking ZnO surface facets from the hydrothermal growth solution.[5,29] As a consequence of these tunable geometric parameters, we have demonstrated the use of this surface-directed assembly process to control material properties in applications including superomniphobic surfaces, photoelectrochemical cells, and anti-biofouling surfaces.[5,29,30,36]

However, despite these promising application examples, to date, the combination of ALD and hydrothermal synthesis for tunable ZnO nanostructure growth has typically only been demonstrated on relatively small sample geometries (<20 cm^2). Therefore, the goal of this study is to demonstrate the ability to maintain this tunability of fabricated ZnO nanostructures on large areas (>120 cm^2) using non-planar (curved) substrates, which would enable their use in new application spaces.

Scaling up the surface-directed assembly process requires modifications to the reactors used for ALD and hydrothermal synthesis. Owing to the self-limiting nature of ALD surface reactions, scaling-up the ALD process is straightforward as it simply requires increasing the chamber volume and adjusting the deposition conditions. Furthermore, there have been significant advances in spatial ALD processes, which can enable further increases in the throughput and scalability of ALD onto

https://doi.org/10.1021/acsaenm.3c00129
ACS Appl. Eng. Mater. 2023, 1, 1583−1592

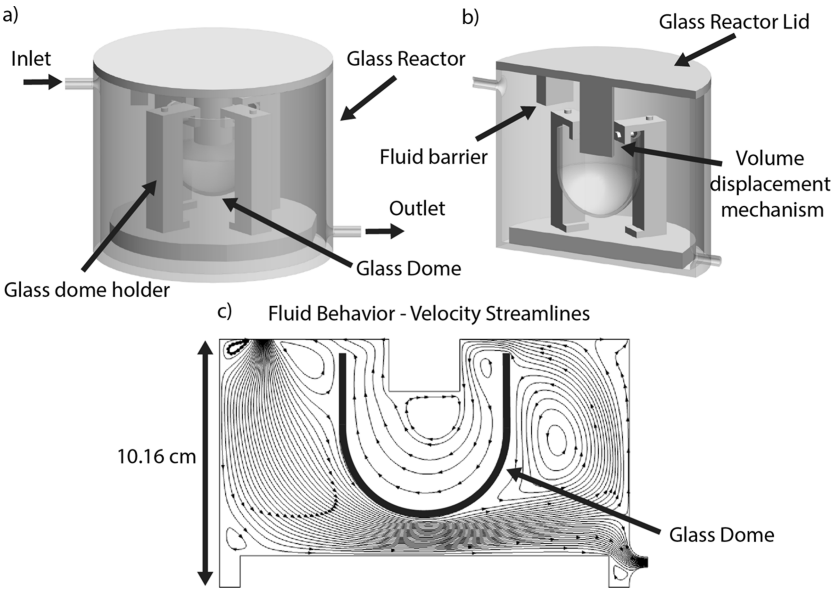

Figure 2. 3D computer-aided design model of glass dome and holder inside the HGS reactor. (a) Front and (b) isometric views of the glass reactor and glass dome holder design. (c) Fluid velocity profile obtained from FEA of the HGS reactor.

large substrates.[37−39] While a range of solution or vapor-phase deposition processes could be used to deposit the seed layer for hydrothermal synthesis, in this study, we focused on ALD because it enables unparalleled conformality and uniformity over 3D structures, as well as the ability to precisely tune the geometric parameters of the resulting ZnO nanostructures by controlling the film crystallographic properties.[28] In contrast, the hydrothermal synthesis process for ZnO NWs is typically performed manually by researchers using laboratory-scale beakers in a batch process. This process suffers from limitations when scaling up the hydrothermal growth onto large, non-planar surfaces, as will be discussed in detail below.

To overcome these limitations, here we introduce the design and construction of an integrated hydrothermal growth system (HGS) based on a customized flow reactor. The HGS allows for programmable control of the solution mass flow rate, as well as spatio-temporal control of the solution temperature in different "zones". The HGS can maintain the tunability of the geometric parameters of the resultant nanostructures, as shown in Scheme 1 (i.e., length d_1, aspect ratio d_1/d_3, orientation θ, and inter-NW spacing d_2) using the surface-directed assembly process.[5,29] Furthermore, this new system enables recirculation of the hydrothermal growth solution, which reduces the chemical waste by 77−92% compared to a single pass flow reactor. We envision that this work will inspire new pathways to inform the scale-up of nanomaterial syntheses onto industrially relevant surface geometries and sizes, without compromising spatial resolution or uniformity. As an example application, we showed that this scaled-up process can be used to manufacture anti-biofouling coatings on a transparent glass dome substrate, opening up pathways for use in ocean sensors and windows.

2. RESULTS AND DISCUSSION

2.1. Automated HGS Design

Figure 1a,b shows a schematic comparison between the manual and the automated hydrothermal synthesis processes. The first important difference between the two processes is the transition from a batch reactor to a flow system. This was motivated by early observations that as we start to scale-up the volume of the batch system, non-ideal growth conditions occur. First, a significant amount of homogeneous precipitation of ZnO nanostructures was observed within the growth solution as the reaction proceeds (Figure S1). This resulted in settlement and attachment of homogeneous precipitates on the surface of the substrate because of the long residence time required for the growth solution in the reactor (>75 min). Additionally, using a single solution with a long residence time also depletes the reactant concentration during the growth process, which will influence the hydrothermal growth kinetics as the reaction proceeds.[40] Furthermore, simply stirring the solution in a batch reactor makes it difficult to control the local solution flow profile over the surface of large, non-planar substrates. This flow behavior can influence the hydrothermal growth process by affecting the local boundary layer thickness and the local solution concentration profile near the growth surface.

Our new automated HGS was designed with the goal of addressing these challenges (Figure 1b,c). First, in order to reduce the residence time of the solution in the reactor, we introduced a solution reservoir. This allows us to decouple the total volume of solution used in the growth process from the volume of the reactor. By controlling the flow rate of the solution (using a peristaltic pump), we can control the residence time of the solution in the reactor. To minimize the time that the solution is at the elevated growth temperature (~90 °C), the solution reservoir is maintained at a lower temperature (70 °C), which significantly reduces the rate of formation of homogeneous precipitates in the solution. A pre-heater was introduced at the inlet to the reactor, which rapidly increases the solution temperature to the targeted growth temperature of ~90 °C. The pre-heater allows us to minimize the time that the solution is at 90 °C, which also suppresses the formation of homogeneous precipitates and the corresponding decrease in the solution concentration. As a consequence, while the solution in the batch reactor process was observed to evolve into an opaque white color by the conclusion of the growth, which indicates visible light scattering from the

https://doi.org/10.1021/acsaenm.3c00129
ACS Appl. Eng. Mater. 2023, 1, 1583−1592

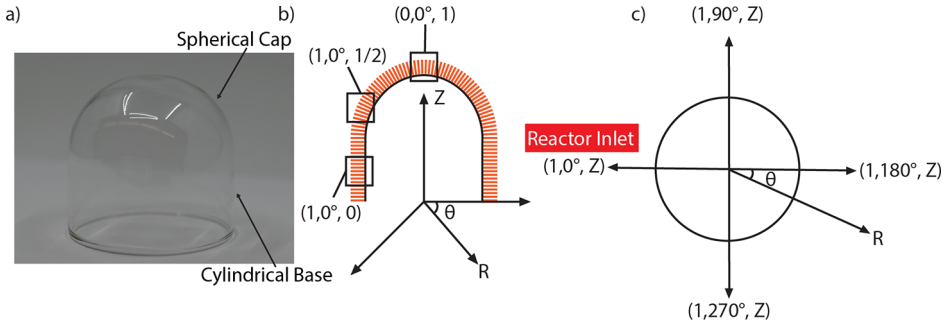

Figure 3. Positions along the surface of the glass dome inside the reactor are defined using a cylindrical coordinate system (R, θ, Z) for the purposes of material characterization. The origin is located at the center of the base, and the closest position to the reactor inlet is defined as (1, 0°, 0). The top of the glass dome is labeled as (0, 0°, 1). R is used to describe the radial position and is defined as 0 along the centroidal axis of the glass dome and as 1 along the perimeter of the cylindrical base. The theta angle, θ, defines the circumferential coordinate. The axial component, Z, is defined as 0, 1/2, or 1 along three vertical positions as shown. (a) Photograph of an uncoated glass dome substrate. (b) Cross-sectional perspective. (c) Top-down (plane-view) perspective.

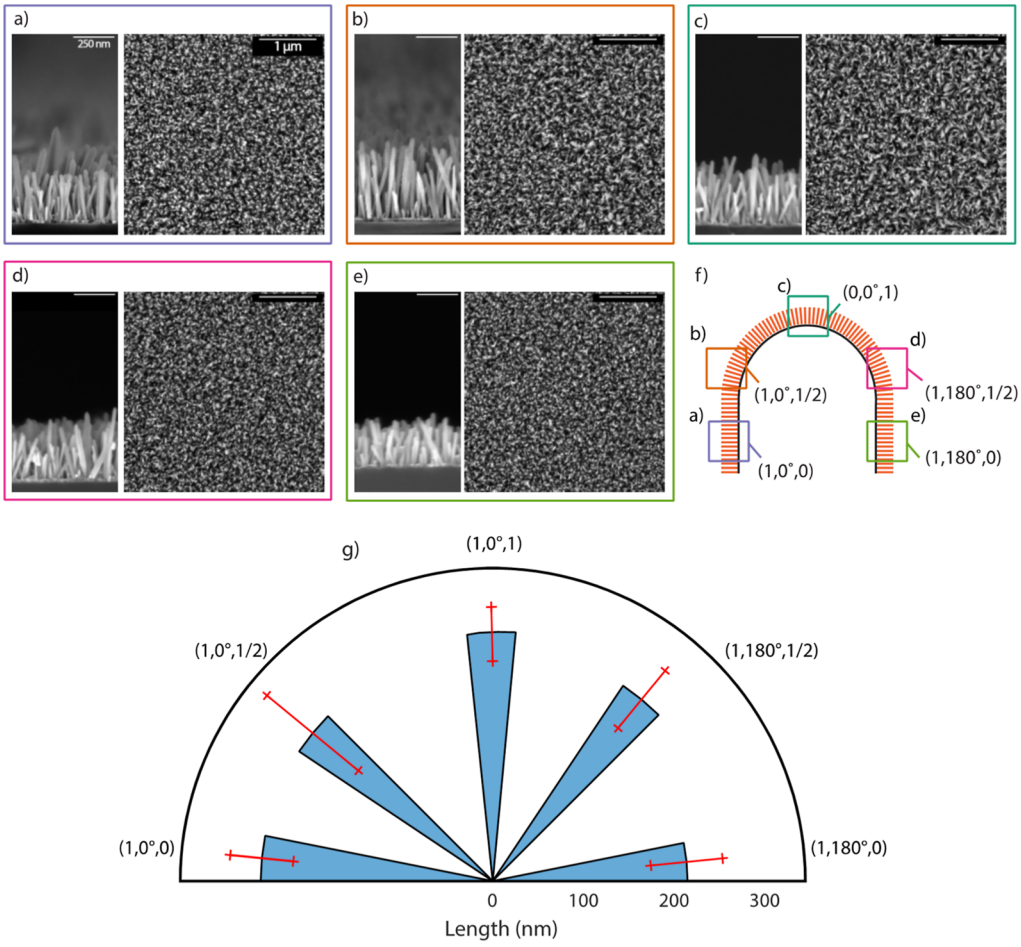

Figure 4. (a–e) ZnO NW length was calculated using SEM images taken at different positions along an arc of the perimeter of the glass dome: (1, 0°, 0), (1, 0°, 1/2), (0, 0°, 1), (1, 180°, 1/2), and (1, 180°, 0). (f) Scheme showing the positions where various SEM images were collected. (g) Radial histogram of NW length at the positions along the arc shown in panel (f). Error bars are based on the measured length of 30 NWs at three different positions.

suspended ZnO nanoparticles in solution, the growth solution in the HGS maintained its initial transparent yellow color throughout the growth.

In addition to controlling the residence time, moving to a flow reactor also allows for improved control of the fluid velocity profile within the reactor. In particular, the reactor geometry can be customized to the size and shape of the desired substrate, which is independent of the total solution volume in the reservoir. As an example, the reactor used in this study was designed to accommodate a curved, glass dome substrate (Figure 2). This substrate was chosen as a model system for the purpose of underwater ocean sensing, where optical sensing equipment must be able to rotate to different viewing angles through a transparent window.[41] The flow

https://doi.org/10.1021/acsaenm.3c00129
ACS Appl. Eng. Mater. 2023, 1, 1583−1592

profile within the reactor will be influenced by both the flow rate and the positioning of the sample within the reactor. Therefore, a customized sample holder and lid were machined to further influence the flow profile. As shown in Figure 2, the glass dome is loaded facedown to reduce the effects of any gravitational settlement of homogeneous precipitates formed in solution. To provide a visual aid, a finite-element simulation of the solution velocity streamlines is shown in Figure 2c (further details are provided in the Experimental Methods section). We note that while a complete fluid dynamics analysis and topology optimization of the reactor geometry are beyond the scope of this study, the ability to influence the flow profile through the design of the reactor highlights the benefits of moving to a flow reactor system to control the uniformity of hydrothermal synthesis over large, non-planar surfaces.

To further improve our spatio-temporal control of the solution flow and temperature profiles, a solution recirculation system was introduced. As shown in Figure 1b, the recirculation of solution within the automated HGS can occur within two loops (further details in Figure S2). The first loop enables recirculation of the solution reservoir while the pre-heater is initially stabilizing its temperature profile to allow the solution at the entrance of the reactor to reach the growth temperature of ∼90 °C. This allows us to reduce the volume of chemical waste produced during the initial transient stages of the temperature equilibration. Stabilization of the pre-heater temperature before introducing the solution into the chamber also reduces non-linearities in the hydrothermal growth kinetics, by ensuring that the solution temperature is always ∼90 °C when the liquid is in contact with the substrate inside the reactor.

A second loop was introduced between the outlet of the reactor and the inlet of the peristaltic pump. This loop allows for partial or complete recirculation of the solution during the growth process. This enables us to reduce chemical waste while maintaining a controlled flow profile through the system. This second loop also allows the solution to partially cool to ∼80 °C when the recirculated liquid is outside the reactor, which reduces the formation of homogeneous precipitates. As a result, the total volume of solution can be decoupled from the reactor volume and residence time, even when completely recirculating the fluid. These two recirculation loops enable the reduction of the chemical waste by 77−92% compared to a single-pass flow reactor. We further note that the solution remained clear when these recirculation loops were employed without the haziness that is characteristic of the formation of homogeneous precipitates in the solution.

2.2. Substrate Geometry and Coordinate System

The glass dome substrate used in this study is shown in Figure 3a. The substrate has a cylindrical geometry at its base and a spherical cap at the top. Therefore, to track the position along the substrate surface during NW characterization, a cylindrical coordinate system (R, θ, Z) was defined (Figure 3b). Scanning electron microscopy (SEM) analysis was performed to characterize the NW growth at nine different positions along the substrate surface. To improve contrast during SEM imaging, small pieces of silicon (Si) were attached to the glass dome in these locations. R is used to describe the radial position, which is defined as 0 along the centroidal axis of the glass dome and 1 along the perimeter of the cylindrical base. The origin is set at the center of the base plane, and the highest point on the glass dome arc position is defined as (0, 0°, 1). Theta, θ, is used to describe the angular coordinate. NW growth was characterized at four orthogonal θ positions (from 0 to 270°). θ = 0° is defined as the angular orientation of the substrate closest to the reactor inlet (Figure 3c). Z is used to describe the vertical position, which was normalized from 0 to 1. Two different Z positions were measured along the cylindrical portion of the substrate (Z = 0 and Z = 1/2) (Figure 3b).

2.3. ZnO NW Characterization—Spatial Uniformity

To quantify the spatial variations in the NW length as a function of position along the glass dome perimeter, SEM analysis was performed. Figure 4 shows cross-sectional SEM images of the ZnO NWs for five different positions along the glass dome: (1, 0°, 0), (1, 0°, 1/2), (0, 0°, 1), (1, 180°, 1/2), and (1, 180°, 0). These positions form the arc of the glass dome that is co-planar with the reactor inlet. The additional data along the circumferential direction are shown in Figure S5. Further details on the image analysis procedures are provided in the Experimental Methods section.

The measured values of NW length are plotted as a radial plot in Figure 4g. As the plot shows, the variation in NW length for positions a−d is within a standard deviation of ±50 nm of the global mean (262 nm). We note that the average length at position e was slightly shorter than the other positions. This can be rationalized based on a visualization of the glass dome surface within the flow pattern (Figure S3). Position e is furthest from both the inlet and the outlet of the reactor and experiences a zone of greater local stagnation in the flow. As a consequence of reduced mass transport, the solution concentration in this position may experience faster depletion of the local reactant concentration. To support this hypothesis, we demonstrated that the average NW length increases as the initial solution concentration increases (Figure S4). This illustrates that, in the future, additional optimization of the reactor geometry could be applied to further improve the flow profile, which would be specific to the targeted substrate geometry for a particular end-use application.

In addition to the NW arrays shown, we also confirmed the ability of the surface-directed assembly process to tune the geometric parameters (inter-NW spacing, NW angular orientation, and growth of nanosheets instead of NWs) by controlling the crystallographic properties and chemical composition of the ALD seed layer (Figure S6). These results demonstrate the power of combining ALD for surface-directed assembly with the scaled-up HGS introduced in this study to programmably control the nanostructure morphology onto large, non-planar surfaces. In the following sections, we demonstrate the ability to use this approach to impart functional properties associated with these nanostructures onto macroscopic surfaces.

2.4. ZnO NW Characterization—Functional Uniformity

To complement to the geometrical uniformity described in the previous section, we also performed optical transmission measurements to study the functional properties of the semiconducting ZnO NW arrays. ZnO is a wide band gap semiconductor (E_g = 3.3 eV), which makes it an attractive functional material for a wide range of optoelectronic and photochemical applications, as described in the Introduction section.[42] Therefore, to quantify the optical properties of the NW arrays fabricated using the HGS system, we developed a platform to measure the uniformity of UV light absorption along the glass dome surface (Figure 5a).

https://doi.org/10.1021/acsaenm.3c00129
ACS Appl. Eng. Mater. 2023, 1, 1583−1592

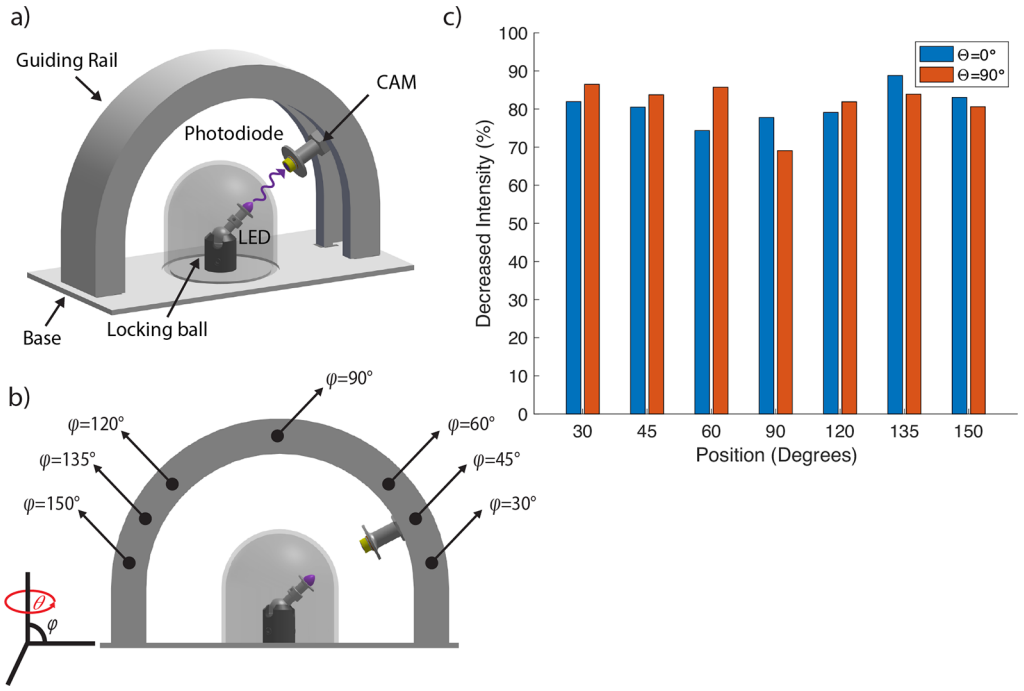

Figure 5. Functional uniformity. (a) Experimental platform used to measure the uniformity of UV light absorption along the glass dome surface. (b) Positions at which the measurements were taken. (c) UV light absorption as a function of position along the surface of the glass dome.

To measure the UV light absorption along the curved glass dome surface, a 375 nm wavelength LED was used as the light source, and a GaP photodiode was used as the receiver. The angular orientation of the LED and the photodiode was aligned along the pathway, and the photodiode response was recorded at different positions along the surface of the glass dome at φ = 30, 45, 60, 90, 120, 135, and 150° (Figure 5b).

To calibrate the data, the photodiode response at each position was initially measured using a clean (uncoated) glass dome. The differential light absorption attributed to the ZnO NWs was then calculated as described in eq 1.

$$\%\ \text{decreased intensity} = \frac{|\text{cleaned GD intensity} - \text{ZnO NWs GD intensity}|}{\text{cleaned GD intensity}} \times 100 \quad (1)$$

Analogous to UV−vis spectrophotometry measurements, this normalization procedure accounts for any slight variation in the relative position of the LED and photodiode along the pathway, as well as variations in the surface geometry of the glass dome along the pathway. To gain further statistical data on the uniformity along the 3D surface, the glass dome was also rotated by θ = 90° along the azimuth angle, and all measurements along the orthogonal pathway were repeated.

The absorption profile along the glass dome surface after NW growth is shown in Figure 5c. For all positions other than the top of the spherical cap (φ = 90°), the variation in intensity is within 82 ± 6%. We note that at φ = 90°, the absorption is slightly lower (69−77%). We hypothesize that this relates to the reduction in the local curvature of the glass dome surface at the top of the spherical cap region, where the cap is not perfectly spherical, and exhibits a locally flat profile (as seen in Figure 3a). This is an artifact of the substrate manufacturing and not indicative of lower uniformity in the NW geometry, as shown from the SEM analysis (Figure 4). Overall, these optical measurements illustrate the potential of the automated HGS to uniformly integrate functional nanostructures onto large, non-planar surfaces. Therefore, in the following section, we explore the use of these nanostructured surfaces for anti-biofouling applications.

2.5. Anti-biofouling Properties of Coated Non-planar Substrates

To demonstrate the ability to impart anti-biofouling properties onto the curved glass dome surface, after growth in the HGS, the NWs along the glass dome surface were functionalized with a low-surface-energy perfluorosilane to generate a superhydrophobic surface. We have previously demonstrated that the addition of a thin (10 nm) Al_2O_3 coating by ALD, followed by silanization, can be used to produce a superhydrophobic surface using the hydrothermal ZnO NW arrays produced from surface-directed assembly.[29] Furthermore, we have shown that these superhydrophobic NW arrays can significantly delay the onset and reduce the rate of biofouling from marine algae.[5] The anti-biofouling performance is attributed to a combination of the formation of a Cassie−Baxter state at the nanostructured liquid/solid interface and a mechanical biocidal effect from the NW geometry.[5]

After completing the HGS growth and silanization processes, a control (uncoated) glass dome and a superhydrophobic NW glass dome were concurrently submerged in the same artificial seawater environment for 2 weeks. This marine algae solution was grown from biomass collected from the coast of Florida 372 (USA), as described in our previous studies.[5,43] Before the beginning of the fouling test, the water repellency was confirmed by measuring the contact angle and contact angle hysteresis of both samples (coated and uncoated glass dome). The superhydrophobic glass dome coated with ZnO NWs exhibited an advancing contact angle of 164 ± 1° and a receding contact angle of 160 ± 1°, resulting in a contact angle hysteresis of 4 ± 1°, confirming its water repellency. In

https://doi.org/10.1021/acsaenm.3c00129
ACS Appl. Eng. Mater. 2023, 1, 1583−1592

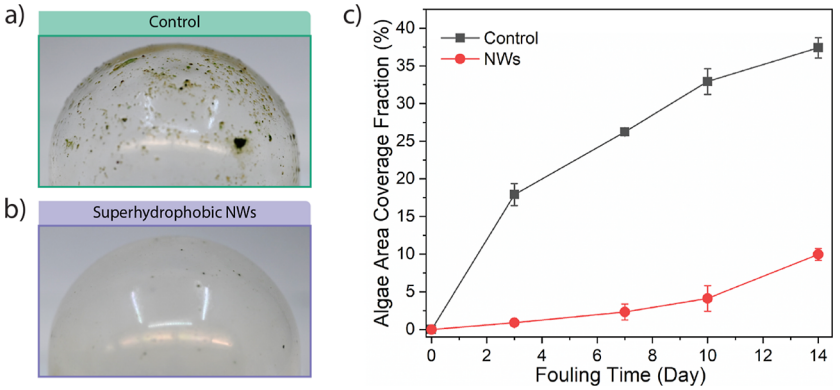

Figure 6. Fouling test on non-planar curved surfaces. (a) Control glass dome after 14 days of the fouling test. (b) Superhydrophobic NW glass dome after 14 days of the fouling test. (c) Algae coverage area as a function of fouling time.

the case of the uncoated (hydrophilic) glass dome, the advancing and receding contact angles were measured to be 57 ± 1 and 0°, thus resulting in a contact angle hysteresis of 57 ± 1°(Figure S7).

Figure 6a,b shows images of the control and the superhydrophobic domes after the fouling test. Optical microscopy analysis was performed on both of the glass domes on day 3, day 7, day 10, and day 14 of the fouling test. Further details on the fouling experiments and characterization are provided in the Experimental Methods section. As observed in Figure 6c, the onset of fouling on the glass dome surface is significantly delayed by the superhydrophobic NWs compared to the control. After day 14, only ~10% of the surface is covered by algae compared to the control, for which ~40% of the surface was covered by algae. This demonstrates the ability to impart multifunctionality onto large, curved, non-planar surfaces coated with superhydrophobic ZnO NWs using the new HGS. In the future, these optically transparent anti-biofouling surfaces can be used for marine applications such as underwater ocean sensors, where curved glass windows are necessary to allow for optical sensing in multiple directions.

3. CONCLUSIONS

In this study, we designed and tested an automated HGS to scale-up the surface-directed assembly process for hydrothermal syntheses of ZnO nanostructures on large, non-planar surfaces. The system was designed to transition the traditional hydrothermal growth process from a batch reactor to a scaled-up flow system, which allows for control of the solution residence time, as well as the spatio-temporal temperature profile. This results in improvements in non-ideal growth conditions such as the formation of homogeneous precipitates in the solution. Additionally, this new system enables recirculation of the hydrothermal growth solution, which reduces the chemical waste by 77−92% compared to a single pass flow reactor.

Using this HGS, we studied the uniformity of the ZnO NWs at different positions along the glass dome surface. In addition to the geometrical uniformity, we also quantified the functional uniformity of the coatings by measuring the UV light absorption along the surface. By functionalizing the NWs, we generated superhydrophobic surfaces, which exhibit anti-biofouling behavior in a marine algae environment.

In the future, the combination of surface-directed assembly using ALD seed layers and the automated HGS can be used for the design and manufacturing of nanostructured surfaces with tunable properties on large, non-planar surfaces. This fabrication platform can be used in a range of applications where nanostructures must be integrated onto industrially relevant surface geometries and sizes. For example, in addition to the examples provided in this study, surface nanostructuring has also been demonstrated to impart multifunctionality in fiber-reinforced composites and tunable optoelectronic properties for applications in solar energy.[30,36,44] To build upon this work, future efforts can further optimize the detailed flow and temperature profile of the reactor for specific target geometries, which could be further informed by computational modeling. We hope that this work will inspire the transition of other nanomaterial synthesis processes to scaled-up, continuous manufacturing platforms to accelerate their commercialization in a range of applications.

4. EXPERIMENTAL METHODS

4.1. Solution Fabrication

The growth solution used during the hydrothermal synthesis was synthesized following a previously reported procedure.[29] All the chemicals were purchased from Sigma-Aldrich. To obtain 1 L of ZnO solution, 25 mM zinc nitrate hexahydrate (molecular weight: 297.49 g/mol) is mixed with 25 mM hexamethylenetetramine (molecular weight: 140.19 g/mol) and 5 mM polyethylenimine, branched (PEI, molecular weight: ~25,000 g/mol) in 1000 mL of deionized (DI) water. To ensure complete dissolution of the solution components, this solution is heated to 95 °C while stirring at 250 rpm. After 30 min, the solution is allowed to cool using a water bath. The solution is then filtrated using a vacuum filtration assembly from Sigma-Aldrich. Three filtration steps (8, 2.5, and 0.22 μm) are performed in series to remove aggregate and particles that have nucleated during the solution preparation process. This solution is stored in a 1 L clean media bottle until the hydrothermal growth process is performed. The pH of the solution is measured using a pH meter, with a pH range between 7.00 and 7.33.

4.2. ALD of Seed Layers

All depositions were carried out in a laboratory-built and hot-walled cross-flow ALD reactor. To provide the initial seed layer for the growth of ZnO NWs, 100 ALD cycles of ZnO are performed on the substrate surface at a temperature of 150 °C and a growth rate of ~2.0 Å/cycle. The chemical precursors used to deposit ZnO are diethylzinc and DI water.

4.3. Scaled-Up Hydrothermal Growth

For the hydrothermal synthesis in the automated HGS, 3 L of the growth solution is heated up to 70 °C while stirring at 400 rpm. After the solution reaches 70 °C, a peristaltic pump (Fisherbrand) is used to flow solution into the pre-heater at a mass flow rate of 0.0036 kg/s.

https://doi.org/10.1021/acsaenm.3c00129
ACS Appl. Eng. Mater. 2023, 1, 1583−1592

The solution is recirculated back to the solution reservoir until the temperature controller reads a temperature of ∼90 °C at the outlet of the pre-heater. A PID temperature controller is used to control and monitor all of the process temperatures (including the temperature at the outlet of the pre-heater T_P and the temperature inside the reactor T_R). Once the temperature controller measures a temperature of ∼90 °C, the solution is directed to the reactor using a three-way valve, where a separate heater is used to maintain the solution temperature inside the glass reactor at ∼90 °C. A customized LabVIEW program is used to monitor and record the process temperatures over time. The substrate is mounted in a holder and placed inside the reactor. In the recirculation mode, the solution is recirculated back to the glass reactor to maintain a constant volume inside the reactor until the hydrothermal synthesis process concludes. The hydrothermal synthesis process is performed for 105 min.

4.4. Finite-Element Modeling

Finite-element analysis (FEA) was performed using COMSOL Multiphysics software. A turbulent flow, low Re $k-\varepsilon$ interface was used to solve the fluid velocity field. The 3D reactor volume was simplified to a 2D slice passing through the centers of both the inlet and outlet ports to reduce complexity and increase the speed of calculation. Since most of the physical system liquid is water, water was selected as the flow region material and was assumed to be incompressible. The temperature of the liquid is assumed to be constant throughout and was set to 20 °C. A "no slip" boundary condition was used for each wall bounding the flow region. A "free surface" boundary was used for the top surface, used assuming a water/air interface. The mass flow rate inlet boundary was set to be 0.0036 kg/s, based on the experimentally measured pump speed. The outlet of the fluid flow region is controlled by pressure and was assumed to be atmospheric pressure while suppressing backflow.

4.5. Scanning Electron Microscopy

A TESCAN RISE SEM was used for plan-view imaging of the ZnO NWs. Cross-sectional images were taken using a TFS Helios 650 Nanolab SEM/FIB microscope. To improve the contrast and avoid excessive charging during SEM analysis, small silicon (Si) pieces (∼7 mm × 7 mm) were attached to the surface of the glass dome using carbon tape. The Si pieces were attached in nine different positions along the glass dome surface as described earlier.

4.6. NW Length Analysis

SEM images were analyzed using the MATLAB platform. The length of 10 different NWs was measured at different positions relative to the center of the cross-sectional SEM image. This procedure was repeated for three different images to generate statistical data for each position.

4.7. UV Transmittance Test

The UV transmittance was recorded at the following positions around the glass dome: degrees 30, 45, 60, 90, 120, 135, and 150°. To record the transmittance at different positions, an arc-shaped guide rail was 3D-printed. A mechanical cam from McMaster-Carr was fastened to the guide rail, with a gallium phosphide (GaP) photodiode (Thorlabs) attached. A 375 nm wavelength LED light was secured to a locking ball and socket mount (Thorlabs) in the middle of the glass dome, and its position was adjusted so that the LED and photodiode were aligned with each other at each position. To calibrate and normalize the data, the photodiode response at each position was initially recorded using the clean glass dome and was then recorded for the NW-coated dome. A second set of measurements was taken after rotating the glass dome by 90°.

4.8. Sample Silanization

Heptadecafluoro-1,1,2,2-tetrahydrodecyltrichlorosilane (F-17) was purchased from Gelest, Inc. Before the silanization process, 60 cycles of Al_2O_3 (thickness = 10 nm) were deposited on top of the ZnO NW surfaces using ALD at a temperature of 150 °C and a growth rate of ∼1.6 Å/cycle. The chemical precursors used to deposit Al_2O_3 are trimethylaluminum and DI water. As we have previously reported, the Al_2O_3 layer serves as a buffer layer and protects the underlying NWs during the silanization process.[5] After the samples are cleaned with oxygen plasma for 20 min, they are exposed to the F-17 silane vapor environment for 24 h at a temperature of 120 °C.

4.9. Superhydrophobicity Testing

The sessile drop method was used to measure the contact angle of the glass domes using a Ramé-Hart contact angle goniometer. Advancing and receding contact angle measurements were taken by measuring the contact angle at which the liquid was slightly added and removed from the sessile liquid drop using the syringe. As the glass dome is a curved surface, most of the measurements were taken near the top of the dome using sessile drops with a volume less than 10 μL to avoid effects from gravity. Various measurements were taken for each glass dome with a standard deviation of ±0.1°.

4.10. Anti-biofouling Testing

The fouling test was performed following the procedure that we have previously reported.[5] Marine algae were raised in a fish tank at room temperature and maintained with a standard bubbler and lighting for 12 h/day. Every week, 40% of the media was replaced with fresh sea water with the food for marine algae, Guillards F/2 (Amazon). Samples were submerged in the media, and optical images were taken on day 3, day 7, day 10, and day 14 using an optical microscope (Nikon). Images were taken at three different positions. The area fraction covered by algae was calculated using ImageJ. Specifically, the optical microscopic images were converted to 8 bit gray images, and the area coverage fraction was obtained by thresholding the images.

■ ASSOCIATED CONTENT

Supporting Information

The Supporting Information is available free of charge at https://pubs.acs.org/doi/10.1021/acsaenm.3c00129.

Experimental methods and relevant results (PDF)

■ AUTHOR INFORMATION

Corresponding Author

Neil P. Dasgupta − *Department of Mechanical Engineering, University of Michigan, Ann Arbor, Michigan 48109, United States; Department of Materials Science and Engineering, University of Michigan, Ann Arbor, Michigan 48109, United States;* orcid.org/0000-0002-5180-4063; Email: ndasgupt@umich.edu

Authors

Alondra M. Ortiz-Ortiz − *Department of Mechanical Engineering, University of Michigan, Ann Arbor, Michigan 48109, United States*

Andrew J. Gayle − *Department of Mechanical Engineering, University of Michigan, Ann Arbor, Michigan 48109, United States*

Jing Wang − *Department of Mechanical Engineering, University of Michigan, Ann Arbor, Michigan 48109, United States*

Hannah R. Faustyn − *Department of Mechanical Engineering, University of Michigan, Ann Arbor, Michigan 48109, United States*

Daniel Penley − *Department of Mechanical Engineering, University of Michigan, Ann Arbor, Michigan 48109, United States*

Caleb Sherwood − *Department of Mechanical Engineering, University of Michigan, Ann Arbor, Michigan 48109, United States*

Anish Tuteja − *Department of Materials Science and Engineering, Department of Macromolecular Science and Engineering, Department of Chemical Engineering, and Biointerfaces Institute, University of Michigan, Ann Arbor,*

https://doi.org/10.1021/acsaenm.3c00129
ACS Appl. Eng. Mater. 2023, 1, 1583−1592

Michigan 48109, United States; orcid.org/0000-0002-2383-4572

Complete contact information is available at: https://pubs.acs.org/10.1021/acsaenm.3c00129

Notes

The authors declare no competing financial interest.

■ ACKNOWLEDGMENTS

This work was supported by DARPA Young Faculty Award D18AP00066. Any opinions, findings, conclusions, or recommendations expressed in this publication are those of the authors and do not necessarily reflect the views of DARPA. This material is based upon work supported by the National Science Foundation under grant no. 1751590. A.M.O.-O. and A.J.G. acknowledge support from the National Science Foundation Graduate Research Fellowship Program under grant no. DGE-1256260. The authors would like to thank Dr. James W. Gose from the Aaron Friedman Marine Hydrodynamics Laboratory at the University of Michigan for providing the marine algae.

■ REFERENCES

(1) Pu, Y. C.; Wang, G.; Chang, K. Der; Ling, Y.; Lin, Y. K.; Fitzmorris, B. C.; Liu, C. M.; Lu, X.; Tong, Y.; Zhang, J. Z.; Hsu, Y. J.; Li, Y. Au Nanostructure-Decorated TiO2 Nanowires Exhibiting Photoactivity across Entire UV-Visible Region for Photoelectrochemical Water Splitting. *Nano Lett.* **2013**, *13*, 3817−3823.

(2) Ahmad, R.; Tripathy, N.; Park, J. H.; Hahn, Y. B. A Comprehensive Biosensor Integrated with a ZnO Nanorod FET Array for Selective Detection of Glucose, Cholesterol and Urea. *Chem. Commun.* **2015**, *51*, 11968−11971.

(3) Laurenti, M.; Cauda, V. ZnO Nanostructures for Tissue Engineering Applications. *Nanomaterials* **2017**, *7*, 374.

(4) Xu, Y.; Wen, W.; Wu, J.-M. Titania Nanowires Functionalized Polyester Fabrics with Enhanced Photocatalytic and Antibacterial Performances. *J. Hazard. Mater.* **2018**, *343*, 285−297.

(5) Wang, J.; Lee, S.; Bielinski, A. R.; Meyer, K. A.; Dhyani, A.; Ortiz-Ortiz, A. M.; Tuteja, A.; Dasgupta, N. P. Rational Design of Transparent Nanowire Architectures with Tunable Geometries for Preventing Marine Fouling. *Adv. Mater. Interfaces* **2020**, *7*, 2000672.

(6) Pan, C.; Zhai, J.; Wang, Z. L. Piezotronics and Piezo-Phototronics of Third Generation Semiconductor Nanowires. *Chem. Rev.* **2019**, *119*, 9303−9359.

(7) Oviroh, P. O.; Akbarzadeh, R.; Pan, D.; Coetzee, R. A. M.; Jen, T. C. New Development of Atomic Layer Deposition: Processes, Methods and Applications. *Sci. Technol. Adv. Mater.* **2019**, *20*, 465−496.

(8) Dong, Y.; Yu, M.; Wang, Z.; Liu, Y.; Wang, X.; Zhao, Z.; Qiu, J. A Top-Down Strategy toward 3D Carbon Nanosheet Frameworks Decorated with Hollow Nanostructures for Superior Lithium Storage. *Adv. Funct. Mater.* **2016**, *26*, 7590−7598.

(9) Wu, Z.-S.; Tan, Y.-Z.; Zheng, S.; Wang, S.; Parvez, K.; Qin, J.; Shi, X.; Sun, C.; Bao, X.; Feng, X.; Müllen, K. Bottom-Up Fabrication of Sulfur-Doped Graphene Films Derived from Sulfur-Annulated Nanographene for Ultrahigh Volumetric Capacitance Micro-Supercapacitors. *J. Am. Chem. Soc.* **2017**, *139*, 4506−4512.

(10) Rubio-Giménez, V.; Galbiati, M.; Castells-Gil, J.; Almora-Barrios, N.; Navarro-Sánchez, J.; Escorcia-Ariza, G.; Mattera, M.; Arnold, T.; Rawle, J.; Tatay, S.; Coronado, E.; Martí-Gastaldo, C. Bottom-Up Fabrication of Semiconductive Metal−Organic Framework Ultrathin Films. *Adv. Mater.* **2018**, *30*, 1704291.

(11) Gregorczyk, K.; Knez, M. Hybrid Nanomaterials through Molecular and Atomic Layer Deposition: Top down, Bottom up, and in-between Approaches to New Materials. *Prog. Mater. Sci.* **2016**, *75*, 1−37.

(12) Ji, X.; Kong, N.; Wang, J.; Li, W.; Xiao, Y.; Gan, S. T.; Zhang, Y.; Li, Y.; Song, X.; Xiong, Q.; Shi, S.; Li, Z.; Tao, W.; Zhang, H.; Mei, L.; Shi, J. A Novel Top-Down Synthesis of Ultrathin 2D Boron Nanosheets for Multimodal Imaging-Guided Cancer Therapy. *Adv. Mater.* **2018**, *30*, 1803031.

(13) Dasgupta, N. P.; Sun, J.; Liu, C.; Brittman, S.; Andrews, S. C.; Lim, J.; Gao, H.; Yan, R.; Yang, P. 25th Anniversary Article: Semiconductor Nanowires - Synthesis, Characterization, and Applications. *Adv. Mater.* **2014**, *26*, 2137−2184.

(14) Zhang, F. Grand Challenges for Nanoscience and Nanotechnology in Energy and Health. *Front. Chem.* **2017**, *5*, 80.

(15) Busnaina, A. A.; Mead, J.; Isaacs, J.; Somu, S.. In *Nanomanufacturing and Sustainability: Opportunities and Challenges BT - Nanotechnology for Sustainable Development*; Diallo, M. S., Fromer, N. A., Jhon, M. S., Eds.; Springer International Publishing: Cham, 2014; pp 331−336.

(16) Fang, F. Z.; Zhang, X. D.; Gao, W.; Guo, Y. B.; Byrne, G.; Hansen, H. N. Nanomanufacturing—Perspective and Applications. *CIRP Ann.* **2017**, *66*, 683−705.

(17) Liddle, J. A.; Gallatin, G. M. Nanomanufacturing: A Perspective. *ACS Nano* **2016**, *10*, 2995−3014.

(18) Oliver, C. R.; Polsen, E. S.; Meshot, E. R.; Tawfick, S.; Park, S. J.; Bedewy, M.; Hart, A. J. Statistical Analysis of Variation in Laboratory Growth of Carbon Nanotube Forests and Recommendations for Improved Consistency. *ACS Nano* **2013**, *7*, 3565−3580.

(19) Pu, X.; Wang, Z. L. Self-Charging Power System for Distributed Energy: Beyond the Energy Storage Unit. *Chem. Sci.* **2021**, *12*, 34−49.

(20) Lupan, O.; Ursaki, V. V.; Chai, G.; Chow, L.; Emelchenko, G. A.; Tiginyanu, I. M.; Gruzintsev, A. N.; Redkin, A. N. Selective Hydrogen Gas Nanosensor Using Individual ZnO Nanowire with Fast Response at Room Temperature. *Sens. Actuators, B* **2010**, *144*, 56−66.

(21) Wu, W.; Wen, X.; Wang, Z. L. Taxel-Addressable Matrix of Vertical-Nanowire Piezotronic Transistors for Active and Adaptive Tactile Imaging. *Science* **2013**, *340*, 952−957.

(22) Xiang, B.; Wang, P.; Zhang, X.; Dayeh, S. A.; Aplin, D. P. R.; Soci, C.; Yu, D.; Wang, D. Rational Synthesis of P-Type Zinc Oxide Nanowire Arrays Using Simple Chemical Vapor Deposition. *Nano Lett.* **2007**, *7*, 323−328.

(23) Tak, Y.; Hong, S. J.; Lee, J. S.; Yong, K. Fabrication of ZnO/CdS Core/Shell Nanowire Arrays for Efficient Solar Energy Conversion. *J. Mater. Chem.* **2009**, *19*, 5945−5951.

(24) Zhang, X.; Huang, X.; Li, C.; Jiang, H. Dye-Sensitized Solar Cell with Energy Storage Function through PVDF/ZnO Nanocomposite Counter Electrode. *Adv. Mater.* **2013**, *25*, 4093−4096.

(25) Xu, S.; Qin, Y.; Xu, C.; Wei, Y.; Yang, R.; Wang, Z. L. Self-Powered Nanowire Devices. *Nat. Nanotechnol.* **2010**, *5*, 366−373.

(26) Wang, Y.; Zhang, Q.; Zhang, C. L.; Li, P. Characterisation and Cooperative Antimicrobial Properties of Chitosan/Nano-ZnO Composite Nanofibrous Membranes. *Food Chem.* **2012**, *132*, 419−427.

(27) Greene, L. E.; Yuhas, B. D.; Law, M.; Zitoun, D.; Yang, P. Solution-Grown Zinc Oxide Nanowires. *Inorg. Chem.* **2006**, *45*, 7535−7543.

(28) Bielinski, A. R.; Kazyak, E.; Schlepütz, C. M.; Jung, H. J.; Wood, K. N.; Dasgupta, N. P. Hierarchical ZnO Nanowire Growth with Tunable Orientations on Versatile Substrates Using Atomic Layer Deposition Seeding. *Chem. Mater.* **2015**, *27*, 4799−4807.

(29) Bielinski, A. R.; Boban, M.; He, Y.; Kazyak, E.; Lee, D. H.; Wang, C.; Tuteja, A.; Dasgupta, N. P. Rational Design of Hyperbranched Nanowire Systems for Tunable Superomniphobic Surfaces Enabled by Atomic Layer Deposition. *ACS Nano* **2017**, *11*, 478−489.

(30) Bielinski, A. R.; Gayle, A. J.; Lee, S.; Dasgupta, N. P. Geometric Optimization of Bismuth Vanadate Core−Shell Nanowire Photoanodes Using Atomic Layer Deposition. *ACS Appl. Mater. Interfaces* **2021**, *13*, 52063−52072.

(31) George, S. M. Atomic Layer Deposition: An Overview. *Chem. Rev.* **2010**, *110*, 111−131.

(32) Elam, J. W.; Routkevitch, D.; Mardilovich, P. P.; George, S. M. Conformal Coating on Ultrahigh-Aspect-Ratio Nanopores of Anodic Alumina by Atomic Layer Deposition. *Chem. Mater.* **2003**, *15*, 3507−3517.
(33) Young, M. J.; Schnabel, H.-D.; Holder, A. M.; George, S. M.; Musgrave, C. B. Band Diagram and Rate Analysis of Thin Film Spinel LiMn2O4 Formed by Electrochemical Conversion of ALD-Grown MnO. *Adv. Funct. Mater.* **2016**, *26*, 7895−7907.
(34) Bozhinov, N.; Blagoev, B.; Marinova, V.; Babeva, T.; Goovaerts, E.; Dimitrov, D. Properties of ALD Aluminum-Doped ZnO as Transparent Conductive Oxide. *Bulg. Chem. Commun.* **2016**, *48*, 193−197.
(35) Zhuiykov, S.; Kawaguchi, T.; Hai, Z.; Karbalaei Akbari, M.; Heynderickx, P. M. Interfacial Engineering of Two-Dimensional Nano-Structured Materials by Atomic Layer Deposition. *Appl. Surf. Sci.* **2017**, *392*, 231−243.
(36) Bielinski, A. R.; Lee, S.; Brancho, J. J.; Esarey, S. L.; Gayle, A. J.; Kazyak, E.; Sun, K.; Bartlett, B. M.; Dasgupta, N. P. Atomic Layer Deposition of Bismuth Vanadate Core-Shell Nanowire Photoanodes. *Chem. Mater.* **2019**, *31*, 3221.
(37) Poodt, P.; Cameron, D. C.; Dickey, E.; George, S. M.; Kuznetsov, V.; Parsons, G. N.; Roozeboom, F.; Sundaram, G.; Vermeer, A. Spatial Atomic Layer Deposition: A Route towards Further Industrialization of Atomic Layer Deposition. *J. Vac. Sci. Technol., A* **2011**, *30*, 010802.
(38) Muñoz-Rojas, D.; MacManus-Driscoll, J. Spatial Atmospheric Atomic Layer Deposition: A New Laboratory and Industrial Tool for Low-Cost Photovoltaics. *Mater. Horiz.* **2014**, *1*, 314−320.
(39) Musselman, K. P.; Uzoma, C. F.; Miller, M. S. Nano-manufacturing: High-Throughput, Cost-Effective Deposition of Atomic Scale Thin Films via Atmospheric Pressure Spatial Atomic Layer Deposition. *Chem. Mater.* **2016**, *28*, 8443−8452.
(40) Podrezova, L. V.; Porro, S.; Cauda, V.; Fontana, M.; Cicero, G. Comparison between ZnO Nanowires Grown by Chemical Vapor Deposition and Hydrothermal Synthesis. *Appl. Phys. A* **2013**, *113*, 623−632.
(41) Delauney, L.; Compère, C.; Lehaitre, M. Biofouling Protection for Marine Environmental Sensors. *Ocean Sci.* **2010**, *6*, 503−511.
(42) Srikant, V.; Clarke, D. On the Optical Band Gap of Zinc Oxide. *J. Appl. Phys.* **1998**, *83*, 5447−5451.
(43) Wang, J.; Wu, B.; Dhyani, A.; Repetto, T.; Gayle, A. J.; Cho, T. H.; Dasgupta, N. P.; Tuteja, A. Durable Liquid- and Solid-Repellent Elastomeric Coatings Infused with Partially Crosslinked Lubricants. *ACS Appl. Mater. Interfaces* **2022**, *14*, 22466−22475.
(44) Rodríguez, R. E.; Lee, T. H.; Chen, Y.; Kazyak, E.; Huang, C.; Cho, T. H.; LePage, W. S.; Thouless, M. D.; Banu, M.; Dasgupta, N. P. Electrically Conductive Kevlar Fibers and Polymer-Matrix Composites Enabled by Atomic Layer Deposition. *ACS Appl. Polym. Mater.* **2021**, *3*, 5959−5968.

https://doi.org/10.1021/acsaenm.3c00129
ACS Appl. Eng. Mater. 2023, 1, 1583−1592